Additive Manufacturing Letters 3 (2022) 100099

Contents lists available at ScienceDirect

Additive Manufacturing Letters

journal homepage: www.elsevier.com/locate/addlet

In situ detection of cracks during laser powder bed fusion using acoustic emission monitoring

Mikhail Seleznev[a,*], Tobias Gustmann[b], Judith Miriam Friebel[c], Urs Alexander Peuker[c], Uta Kühn[b], Julia Kristin Hufenbach[b,d], Horst Biermann[a], Anja Weidner[a]

[a] Institute of Materials Engineering, Technische Universität Bergakademie Freiberg, Gustav-Zeuner-Straße 5, 09596 Freiberg, Germany
[b] Institute for Complex Materials, Leibniz-Institut für Festkörper- und Werkstoffforschung Dresden, Helmholtzstraße 20, 01069 Dresden, Germany
[c] Institute of Mechanical Process Engineering and Mineral Processing, Technische Universität Bergakademie Freiberg, Agricolastraße 1, 09599 Freiberg, Germany
[d] Institute of Materials Science, Technische Universität Bergakademie Freiberg, Gustav-Zeuner-Straße 5, 09596 Freiberg, Germany

ARTICLE INFO

Keywords:
Additive manufacturing
Laser powder bed fusion
Aluminium alloy
Acoustic emission
X-ray computed tomography
Monitoring
Crack detection

ABSTRACT

Despite rapid development of laser powder bed fusion (L-PBF) and its monitoring techniques, there is still a lack of in situ crack detection methods, among which acoustic emission (AE) is one of the most sensitive. To elaborate on this topic, in situ AE monitoring was applied to L-PBF manufacturing of a high-strength $Al_{92}Mn_6Ce_2$ (at. %) alloy and combined with subsequent X-ray computed tomography. By using a structure borne high-frequency sensor, even a simple threshold-based monitoring was able to detect AE activity associated with cracking, which occurred not only during L-PBF itself, but also after the build job was completed, i.e. in the cooling phase. AE data analysis revealed that crack-related signals can easily be separated from the background noise (e.g. inert gas circulation pump) through their specific shape of a waveform, as well as their energy, skewness and kurtosis. Thus, AE was verified to be a promising method for L-PBF monitoring, enabling to detect formation of cracks regardless of their spatial and temporal occurrence.

1. Introduction

Among various methods of metal additive manufacturing (AM), laser powder bed fusion (L-PBF) is one of the dominating techniques industrially used techniques [1,2]. The main L-PBF defect types – balling, porosity, lack of fusion and fusion holes, cracks – are typically the result of non-optimal building parameters [3], which have to be set individually for each machine type and alloy. Unlike ex situ analyses of a manufactured part, in situ monitoring of AM enables immediate adjustment of processing parameters, which is very efficient in terms of time and material savings. Therefore, the development of in situ monitoring techniques for metal-based AM is nowadays in the focus of interest [4]. Most monitoring methods are camera-based and provide information mainly from the melt pool [5]. This allows to detect defects which form in the upper layer, such as balling, lack of fusion or gas pores. However, cracking can take place not only in the upper layer [6], but at any position of the manufactured part due to residual stresses and temperature gradients [7]. Thus, in order to detect any crack, a method is required that is not limited to the upper layer, such as the method of acoustic emission (AE).

AE is an elastic wave emitted by a localized change in stress, e.g., due to a crack, a twin or a shear band formation [8]. The AE method is therefore ideal for detecting cracks and is used in materials science and industrial monitoring, including AM [9]. AM monitoring has been significantly improved in recent years through the use of machine learning (ML) [10], including AE-based methods [11]. Most commonly, researchers use airborne AE sensors (microphones) for defect detection at a frequency range of 0 – 100 kHz [11–14]. With such an AE setup, processes in the melt pool [14] (including pore formation [15]) can be detected. However, fast events in a solidified metal (e.g. cracks) naturally produce AE with higher frequencies [16]. The use of high-frequency structure-borne AE sensors thus makes it possible to detect cracks in situ during L-PBF [17]. However, the related works focus on finding relationships between AE data streams and key processing conditions (e.g. low power, optimum power, high power) rather than the defects themselves [18]. The aim of the present work is therefore a direct correlation between the observed cracks formed during L-PBF and the registered AE signals. For this purpose, in situ AE monitoring of the L-PBF process was cross-linked with the information from the machine protocol and the ex situ X-ray micro-computed tomography (μCT) of the manufactured samples and then jointly analyzed.

2. Experimental methods

A metastable $Al_{92}Mn_6Ce_2$ (at. %) alloy suitable for L-PBF was selected as an experimental material due to the well-studied relation be-

* Corresponding author.
E-mail address: mikhail.seleznev@iwt.tu-freiberg.de (M. Seleznev).

https://doi.org/10.1016/j.addlet.2022.100099
Received 25 July 2022; Received in revised form 25 October 2022; Accepted 31 October 2022

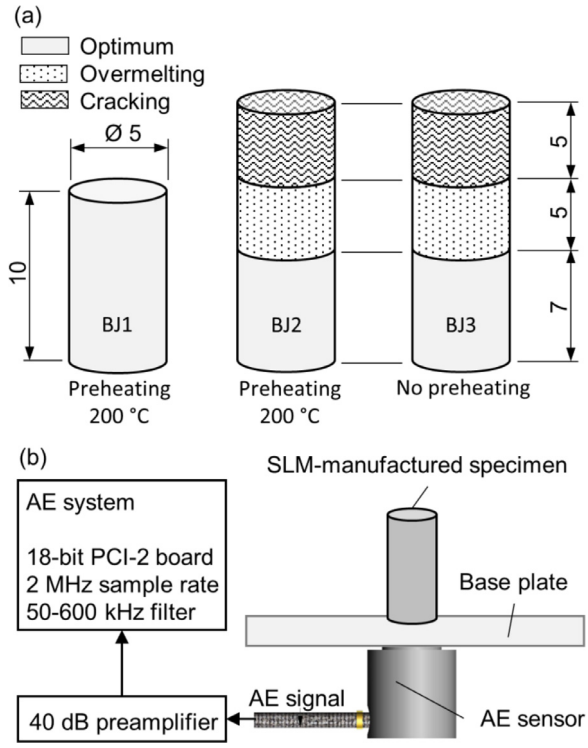

Fig. 1. (a) Geometric dimensions of the three samples (BJ1, BJ2, and BJ3) intended for additive manufacturing by L-PBF using three build parameter presets (sizes are given in mm). (b) Schematic diagram of the acoustic emission setup.

tween manufacturing parameters, defects, microstructure, and material properties [19]. The alloy was gas-atomized (EIGA: Electrode Induction Melting Inert Gas Atomization, Eckart TLS GmbH) to a powder with a median diameter $d_{50} = 35$ µm and processed in a SLM280 2.0 Dual Laser machine (SLM Solutions Group AG). Cylindrical samples with a diameter of 5 mm were manufactured under argon atmosphere with a constant laser power of 250 W, a hatch distance of 0.1 mm and a layer thickness of 50 µm (stripe scanning pattern, 79° vector rotation). By varying the laser scanning speed between 500, 850, and 1150 mm/s, three manufacturing conditions were established based on previous findings: overmelting, optimum, and cracking, respectively. In total, three samples were built in three different build jobs (**Fig. 1a**). Build job 1 (BJ1), which refers to the reference state, consisted of a cylinder of 10 mm height manufactured with optimal parameters and preheating of the baseplate to 200°C. Build job 2 (BJ2) consisted of a combination of all three parameter presets and the same preheating step. Finally, build job 3 (BJ3) was similar to BJ1, but was carried without preheating of the baseplate. All samples were built on an Al baseplate ($98 \times 98 \times 10$ mm^3), which was mounted on the in-house customized building frame.

The AE waveforms were acquired using the PCI-2-based AE system from Physical Acoustics Corp. (USA) according to the scheme shown in **Fig. 1b**. The broadband high temperature AE sensor D9215 was attached to the baseplate directly below the manufactured sample using the high temperature grease Molykote ® 41 as a coupling medium. The AE signal was amplified by 40 dB with the low-noise preamplifier, passed through the 50–600 kHz band-pass filter and recorded by the 18-bit PCI-2 board with a sampling frequency of 2 MHz. AE signals with an amplitude above the specified threshold level (90-100 dB) were recorded with a fixed 4k length and displayed on site using the "AE Viewer" software integrated in the AE system. The threshold level was set individually before each AM session so that it was just above the amplitude of the background noise. AE monitoring was carried out throughout the AM process and two hours after the completion of the AM job to detect possible cracking activity during cooling of the sample.

Signal processing and analysis were performed using the Python programming language. The power spectral density of the waveform of an AE event was calculated with the fast Fourier transform according to Welch method [20] and then normalized. In addition, statistical features such as root mean square (RMS), skewness γ_x and kurtosis k_x (3rd and 4th standardized distribution moments, respectively) were calculated as following:

$$RMS = \sqrt{\frac{\sum_{i=1}^{n}(x_i - \mu_x)}{n-1}}, \quad (1)$$

$$\gamma_x = E\left(\frac{x-\mu_x}{\sigma_x}\right)^3, \quad (2)$$

$$k_x = E\left(\frac{x-\mu_x}{\sigma_x}\right)^4, \quad (3)$$

where E is a mathematical expectation, x is an AE amplitude of a waveform time series, μ_x is the mean and σ_x is the standard deviation of x.

Non-destructive and three-dimensional imaging via µ-CT was used to characterize the manufactured samples using previously obtained experience of the authors with Al alloys [21]. All scans were performed with a Zeiss Xradia Versa 510 (Carl Zeiss, Germany) µ-CT at a power of 10 W and a voltage of 160 kV and the highest possible resolution of 2.85 µm (voxel size). Due to the aspect ratio of the samples being in the range of 3 to 4, data stitching of either three or four separate field of view scans was performed. For each scan, 1601 projections were taken over the range of 360° with an exposure time of 5 s.

The acquired µ-CT data were reconstructed with the filtered back-projection algorithm within the "Scout-and-Scan" software by Zeiss. Image processing after reconstruction was performed using the freeware "Fiji ImageJ" and the software "Dragonfly" from Object Research Systems (Canada). The segmentation of the volume between matrix and defect (crack or pore) was achieved by thresholding the intensity of the voxels. Further, only the continuous crack space was extracted and used for the visualization of the cracks.

3. Results and discussion

3.1. X-ray computed tomography

After processing of the raw µ-CT data, radial sections (slices) with a step size of 1 °were obtained and analyzed. Careful inspection of each slice revealed cracks with crack opening of at least 2.85 µm (voxel resolution). Selected slices of the individual sample scans are shown in **Fig. 2b, c, e**. In addition, crack voxels were extracted from the scanned volume (see Section 2 for details) and shown separately in **Fig. 2a, d, f**. Further µ-CT crack projections from different angles can be found in the **supplementary**.

As expected, the reference sample BJ1 has the best integrity. However, despite the optimal L-PBF processing parameters, there is one crack at a height of 4 mm (**Fig. 2a, b**). There are possibly further cracks located in the area near the baseplate, but this part of the sample was unfortunately lost during cut-off.

Sample BJ2 clearly shows three areas related to three build parameters. The lower part looks similar as that of a BJ1 with a side crack. The crack extraction showed that it actually consists of three cracks: two smaller cracks slightly above and one below the main one (**Fig. 2c, d**). Another faint crack can be seen arising from the cut-off area. The middle of BJ2 contains significant residual porosity, which is due to the intensive evaporation in the melt pool caused by the selected manufacturing presetting "overmelting". However, no cracking was found to emerge from this area. The upper part of BJ2, which was manufactured using lower energy, contains two big cracks. One of them is located in the middle of "cracking" area. Another was initiated right at the border of the "overmelting" area and went through it, deviating from a flat path.

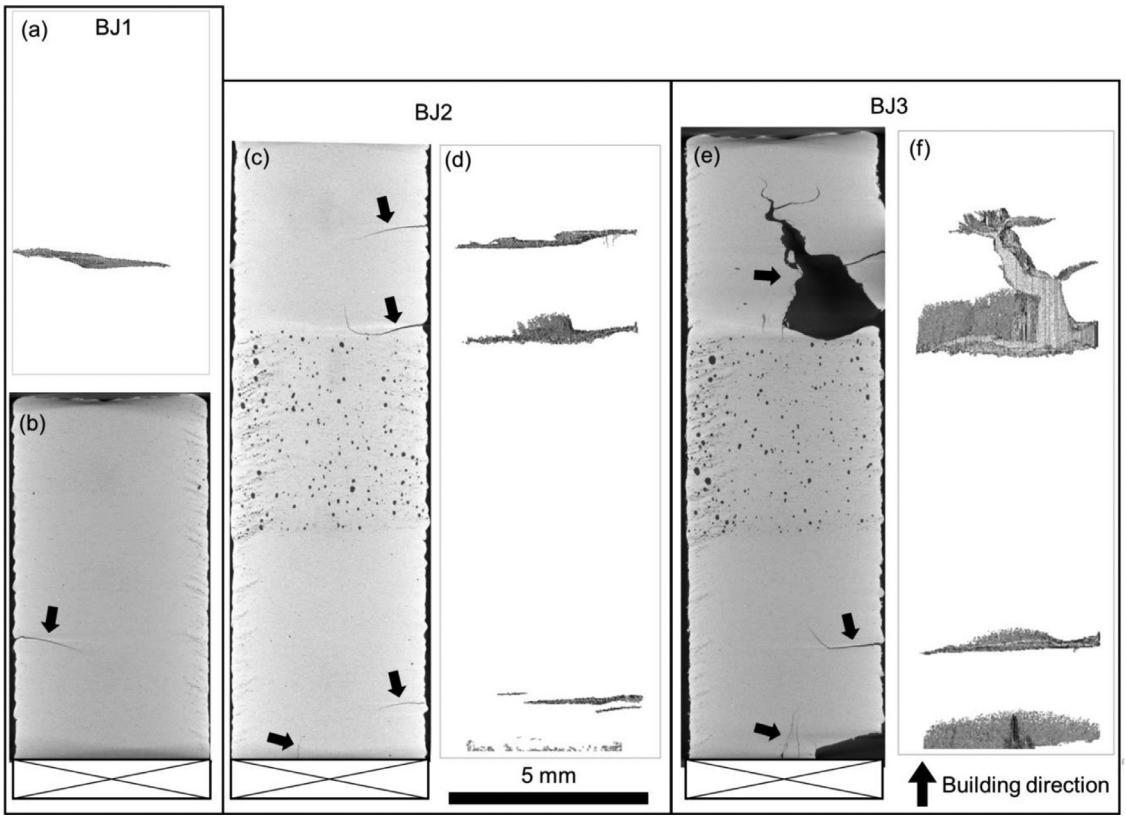

Fig. 2. Selected μ-CT cross sections of the three $Al_{92}Mn_6Ce_2$ samples, manufactured by L-PBF according to the plan shown in Fig. 1**a**: Raw data (b, c, e) and filtered cracks (a, d, f). Crossed rectangles at the bottom of each sample correspond to the cut-off part. Arrows point on detected cracks.

It seems that this deviation was caused by an attraction of the crack tip on residual pores directly connected to the crack.

As expected, the lack of preheating during BJ3 resulted in severe cracking and loss of a sample fragment near the baseplate (Fig. 2**e, f**). Surprisingly, the upper part of BJ3 was also affected by the absence of preheating. Large size and entanglement of cracks hinder determination of their exact number in both lower and upper parts of BJ3. Nevertheless, high AE activity is to be expected in these two parts.

3.2. Acoustic emission

During the set-up of the AE system, sample signals were recorded prior to the L-PBF process under different conditions (power on/off, powder rake movement, pump on/off, etc.). No significant influence of the activity of the machine modules on the AE was found, except for the work of the inert gas circulation pump. The noise amplitude of the AE was 10 times higher (2 against 0.2 V) when the pump was turned on (Fig. 3). Since L-PBF requires a constant flow of inert gas and circulation during processing, the vibrations of the built-in pump were unavoidable.

Due to its stable amplitude level, most of the pump-related background noise was cut off from the recorded AE signals by a constant threshold value. However, some of the noise bursts exceeded the threshold, which was set to be as low as possible. In general, all AE signals recorded during the three experiments belonged to one of four types (Fig. 4). The AE signals of the background noise contained either a group of continuous bursts (Fig. 4**a**) or a single burst (Fig. 4**c**), but had a similar power spectrum (Fig. 4**b, d**). Several noise bursts were of a different nature (probably a hardware switcher) and contained higher frequencies in the spectrum (Fig. 4**e, f**). However, all three types of noise signals occurred not only during L-PBF processing, but also separately from it during AE setup. This means that they are independent of the AM process.

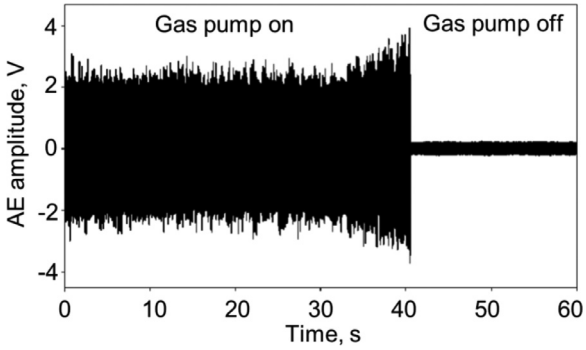

Fig. 3. AE waveform recorded during operation and shutdown of the inert gas circulation pump in the L-PBF machine.

The AE signals of the fourth type were assumed to originate from developing cracks due to their specific characteristics: triangular waveform with immediate peak rise and gradual decay during 1 to 3 ms (Fig. 4**g**). Most of the crack-related AE signals had a peak power at a frequency of 100 kHz and a significant part of the spectrum in the high frequency range up to 500 kHz (Fig. 4**h**). In addition to the specific waveform, an AE signal of a crack had a specific sound that can be converted to a human-accessible range by reducing the playback speed. A larger set of collected AE signals is provided in the **supplementary** along with reproducible audio files for each signal.

One can notice a similarity between the normalised PSD distributions of a crack and an AE signal with noise burst (Fig. 4**f, h**). This is the main reason for inapplicability of PSD-based k-means clustering according to E. Pomponi and A. Vinogradov [22]. Nevertheless, registered crack signals can be easily separated from the noise by their specific waveform

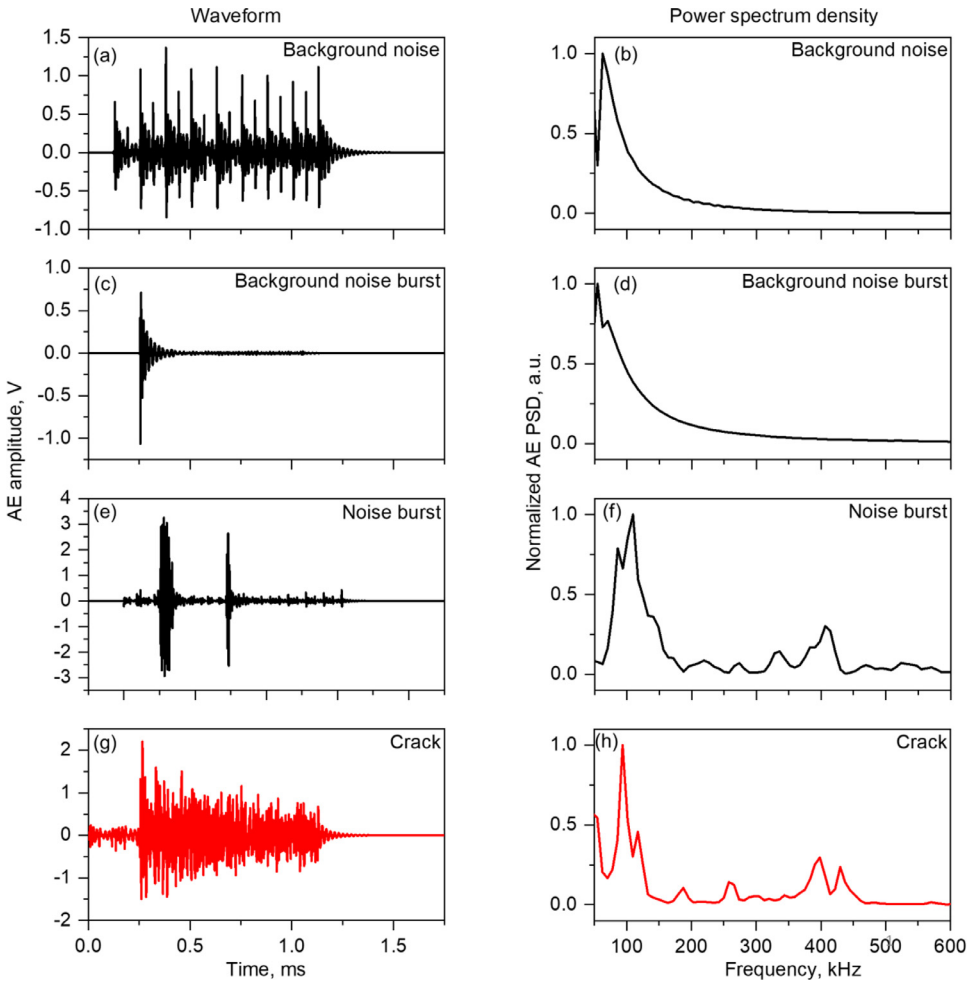

Fig. 4. Examples of four types of recorded acoustic emission signals, taken from the BJ2: background noise (a, b), background noise burst (c, d), noise burst (e, f), and crack (g, h, red color). Normalized power spectral density (b, d, f, h) was calculated for each waveform (a, c, e, g) of an event. Audio examples of each event type can be found in the **supplementary**.

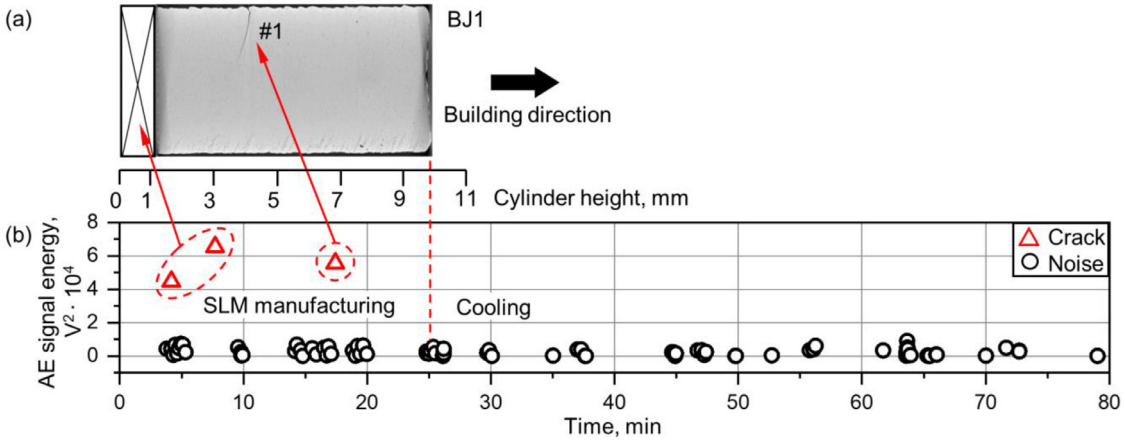

Fig. 5. µ-CT (a) and AE (b) data synchronized with each other along the time scale during the BJ1. Arrows indicate correlation between registered AE crack events (red triangles) and crack locations of the sample.

without additional calculations. Such a manual separation serves as the reference with the aim to develop an automated classification routine in a future work.

3.3. Joint analysis of L-PBF, µ-CT and AE data

After detecting cracks in a µ-CT scan and crack signals in AE data, both were synchronized using the time scale from the log file of the AM machine. The results of the first build job are represented in Fig. 5. Only three crack signals were detected. Two crack signals on 5th and 8th minute of manufacturing seem to correspond to cracks near the base-plate in the cut-off part. The revealed crack #1 at a height of 4 mm seems to correspond to the AE signal recorded in the 18th minute. The delay between the manufacturing of a cracked layer and the corresponding AE signal is 8 minutes, indicating that cracking occurred during the cooling of this layer far below the melt pool and associated thermal oscillations.

Following the same procedure, all four crack locations in the sample of the build job #2 are associated with a certain AE activity (Fig. 6).

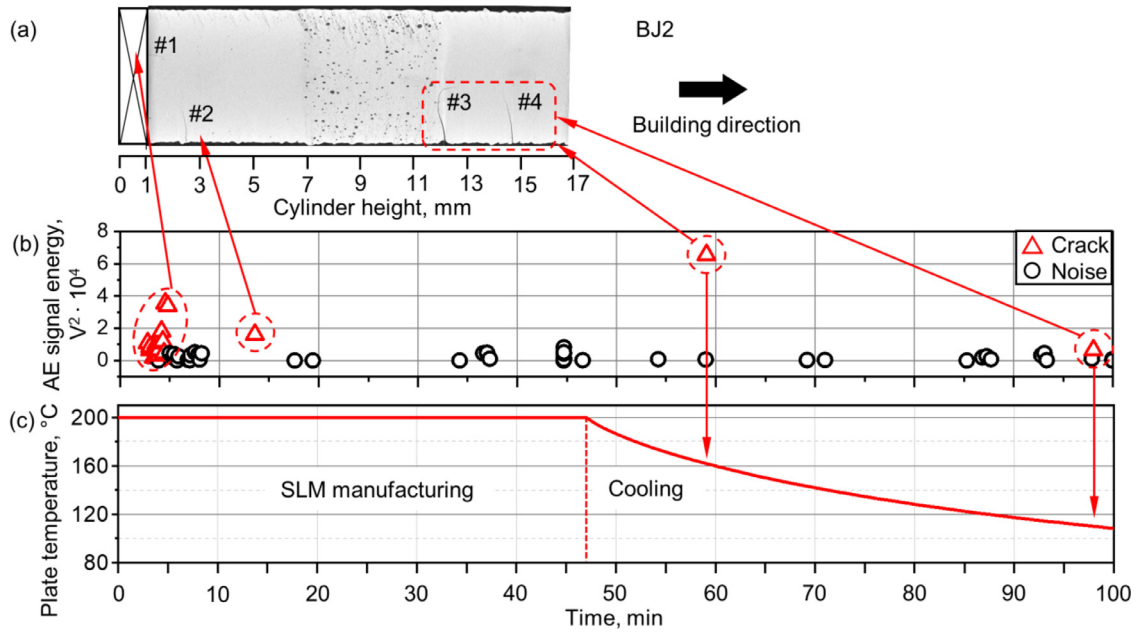

Fig. 6. µ-CT (a), AE (b), and baseplate temperature (c) data synchronized on the time scale during BJ2. Arrows indicate the correlation between registered AE crack events (red triangles) and crack locations of the sample.

The first 15 crack signals refer to the area close to the baseplate, of which only one crack (#1) remained after cut-off. Crack #2 was formed 5 minutes after the completion of the respective layer, as shown by the following AE signal. Although crack site #2 consisted of three cracks, only one AE signal was detected. This means that either all the three cracks occurred simultaneously or the signals from two smaller cracks were below the detection threshold. According to the last two AE signals, cracks #3 and #4 occurred already after the manufacturing was completed during the cooling of the sample (**Fig. 6c**). Although it is not clear which crack of #3 and #4 belongs to which AE signal, the delay between the completion of the corresponding layer and the appearance of the crack was 18-25 and 58-65 minutes, respectively, for each AE signal. This observation demonstrates that in addition to the manufacturing process, cooling also plays an important role in the quality of L-PBF and should also be monitored.

As expected, the high number of cracks in the sample of build job #3 correlate with the high number of AE signals (**Fig. 7**). Due to the lack of pre-heating, the time between the layer build-up and crack formation was not very long, as the material needed much less time to cool down. Due to the high number and entanglement of cracks, it is not possible to assign a corresponding AE signal to each crack. However, both cracks and AE signals form two large groups that are interconnected. In contrast to the build job #1, build job #3 is characterized by a large number of low energy signals, emitted by relatively small cracks, in accordance with the basic relationship between the energy of the AE signal and the defect size [23]. The registration of all crack signals, including those with a signal-to-noise ratio SNR < 1, requires, however, threshold-free AE monitoring and analysis, which is the goal of future work.

3.4. Statistical analysis of AE signals

As can be seen from the plots of AE energy versus time (**Fig. 5b, 6b, 7b**), most of the noise can be cut-off by setting a threshold AE signal energy of 10^4 V^2. This preserves the main AE signals emitted by the cracks detected by µ-CT, while supressing the low-energy signals associated with microcracks. In order to find a basis for future automated threshold-free classification of signals (and thus avoid high computational costs) one can look for statistical parameters commonly used for signal analysis [11]. Among the other parameters, three were most meaningful in the present case: root mean square (RMS), skewness and kurtosis (calculated according to **Eqs. 1-3**) of the time series of the signals (**Fig. 8**). The distribution of the RMS is similar to that of a signal energy: all noise signals have an RMS below 0.4 V, while most detrimental cracks emit signals with higher values (**Fig. 8a-c**). The scatterplot of the skewness vs. kurtosis axes clearly shows that all the crack-related AE signals are in a tiny area close to zero, i.e. they have minimal 3rd and 4th standardized moments (**Fig. 8d-f**). Expressed in numbers, crack signals range from 0 to 15 for the kurtosis and from - 0.4 to 0.5 for the skewness.

3.5. Analysis of cracks

The observed cracks and ways to avoid them can be categorized as following:

- In all three experiments, cracks occurred at the interface between the baseplate and the sample. Thus, the use of support structures is strongly recommended, not only to facilitate the removal of the manufactured parts, but also to avoid their possible damage due to cracking.
- The strong cracking in BJ3 shows that a preheating of at least 200 °C is required to produce crack-free parts. This temperature is in good agreement with the behaviour of thermal volume expansion parameter of aluminium, which increases sharply from 20 to 200 °C [24]
- Cracks between “overmelting” and “cracking” zones in BJ2 and BJ3 can be avoided by using one set of manufacturing parameters within one build job.
- The delayed cracking occurred not only during manufacturing (cracks at 3-4 mm height in all samples) but also during cooling (such as cracks #3 and #4 in BJ2). A high cooling rate or thermal gradients do not seem to be the cause, as both parameters are much higher near the melting pool where no cracking was observed. The reason for cracking lies in the mechanical properties of an alloy, which becomes harder (and, consequently, more fragile) with increasing cooling rate [19]. Since not a single crack was observed in the “overmelting” region, it can be recommended to adjust the “optimal” manufacturing parameters to a higher energy input in order to avoid delayed cracking.

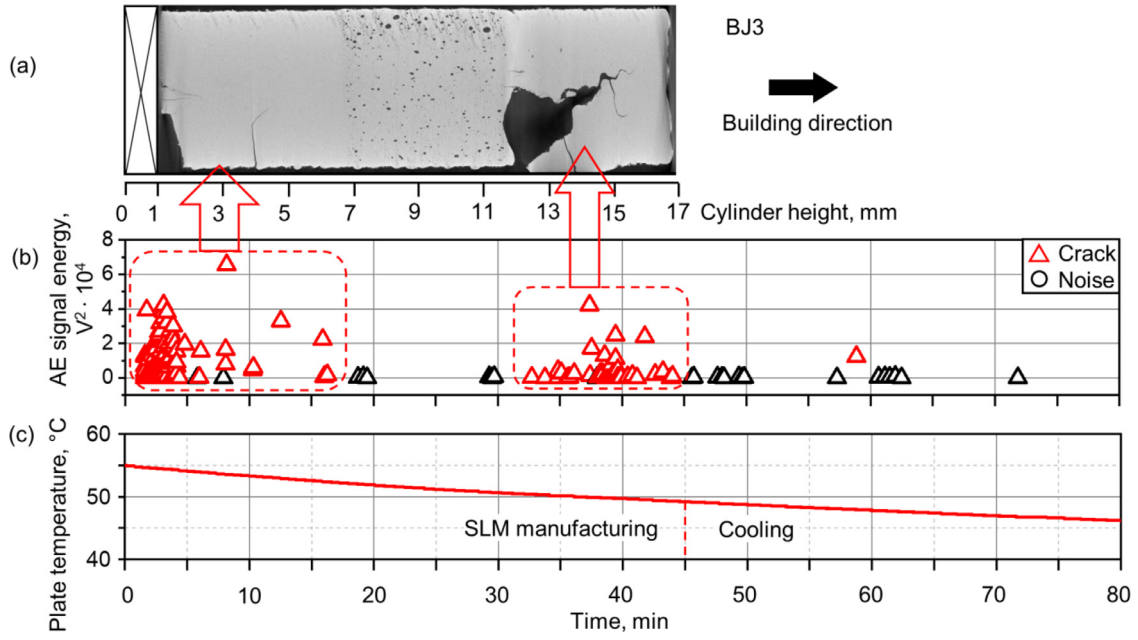

Fig. 7. μ-CT (a), AE (b), and baseplate temperature (c) data synchronized on the time scale during BJ3. Arrows indicate correlation between registered AE crack events (red triangles) and crack sites of the sample.

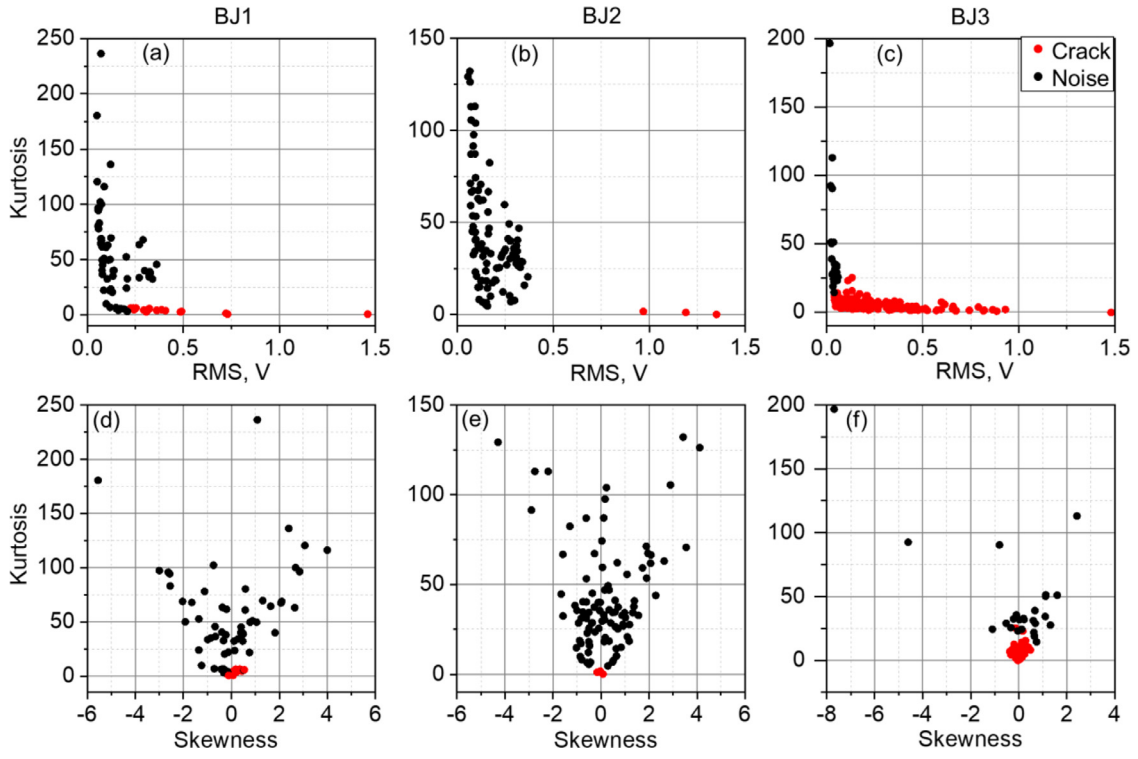

Fig. 8. Distribution of the registered AE signals in terms of crack (red points) and noise (black points) within the parameters RMS, kurtosis, and skewness.

Finally, the analysis of the AE data in relation to μ-CT shows that not all cracks can be detected with a threshold method (ex. triple crack #2 in BJ2). Thus, to capture the total cracking activity, one should either reduce the noise (e.g. by isolating the circulation pump by reinstallation it outside of the AM machine), or process AE data without a threshold. For an efficient monitoring of L-PBF processes using the AE method, both threshold and stream approaches would benefit greatly from the use of a machine learning (ML) algorithm. Based on the findings of the present study, ML can efficiently implement parameter-based rules for in situ classification and clustering of incoming AE data. Therefore, the implementation of ML to the planned AE monitoring system of L-PBF is the goal of future work.

4. Conclusions

In the present work, in situ AE monitoring of L-PBF manufacturing of a high-strength $Al_{92}Mn_6Ce_2$ alloy was combined with ex situ X-ray

micro-computed tomography. After joint data processing and analysis, the following conclusions can be drawn:

- Although the built-in inert gas circulation pump of the L-PBF machine significantly increases the noise level, it is still possible to register the AE activity related to cracking using a simple threshold approach.
- AE signals related to cracking can be easily distinguished from noise signals not only by a certain shape of the waveform but also by statistical parameters such as signal energy, RMS, skewness and kurtosis of the time series.
- There is a clear relation between the cracks directly observed with μ-CT and the AE signals. A significant proportion of the crack signals occur in the first five minutes after the initialization of the build job and correspond to the formation of cracks close to the baseplate.
- The time between built-up of a particular layer and the appearance of a crack can take up to an hour after the completion of the AM build, indicating that, in addition to the manufacturing process, cooling also plays an important role in the quality of L-PBF components and should also be monitored.
- Conventional methods of in situ monitoring of L-PBF usually focus on the melt pool, i.e. currently fabricated layer, and are not able to detect a crack with delayed formation. In contrast, the AE method allows the detection of cracks regardless of their spatial and temporal location.

In general, the obtained results have shown that even a simple threshold-based AE monitoring with a structure-borne high frequency sensor is sufficient and suitable for in situ detection of cracks that occur not only during the additive manufacturing process itself, but also afterwards during cooldown. The detection of micro-cracks with SNR < 1 requires threshold-free AE monitoring and more costly data processing, which is in the goal of future work.

Funding

This work was performed under no additional funding.

Declaration of Competing Interest

The authors declare that they have no known competing financial interests or personal relationships that could have appeared to influence the work reported in this paper.

Data availability

Data will be made available on request.

Acknowledgments

The authors would like to thank Prof. A. Vinogradov (Norwegian University of Science and Technology) for fruitful discussion. In addition, we thank U. Biscop and D. Becker (Leibniz IFW Dresden) for their excellent support in the development of the AE building frame.

Supplementary materials

Supplementary material associated with this article can be found, in the online version, at doi:10.1016/j.addlet.2022.100099.

References

[1] G. Gong, J. Ye, Y. Chi, Z. Zhao, Z. Wang, G. Xia, X. Du, H. Tian, H. Yu, C. Chen, Research status of laser additive manufacturing for metal: a review, J. Mater. Res. Technol. 15 (2021) 855–884, doi:10.1016/j.jmrt.2021.08.050.
[2] T. Wohlers, R.I. Campbell, R. Huff, O. Diegel, J. Kowen, Wohlers Report 2019: 3D Printing and Additive Manufacturing State of the Industry, Wohlers Associates, Colorado, 2019.
[3] B. Zhang, Y. Li, Q. Bai, Defect formation mechanisms in selective laser melting: a review, Chinese J. Mech. Eng. (English Ed. 30 (2017) 515–527, doi:10.1007/s10033-017-0121-5.
[4] X. Lin, K. Zhu, J.Y.H. Fuh, X. Duan, Metal-based additive manufacturing condition monitoring methods: from measurement to control, ISA Trans. 120 (2022) 147–166, doi:10.1016/j.isatra.2021.03.001.
[5] S.K. Everton, M. Hirsch, P. Stravroulakis, R.K. Leach, A.T. Clare, Review of in-situ process monitoring and in-situ metrology for metal additive manufacturing, Mater. Des. 95 (2016) 431–445, doi:10.1016/j.matdes.2016.01.099.
[6] H. Ghasemi-Tabasi, C. de Formanoir, S. Van Petegem, J. Jhabvala, S. Hocine, E. Boillat, N. Sohrabi, F. Marone, D. Grolimund, H. Van Swygenhoven, R.E. Logé, Direct observation of crack formation mechanisms with operando Laser Powder Bed Fusion X-ray imaging, Addit. Manuf. 51 (2022) 102619, doi:10.1016/j.addma.2022.102619.
[7] M.F. Zaeh, G. Branner, Investigations on residual stresses and deformations in selective laser melting, Prod. Eng. 4 (2010) 35–45, doi:10.1007/s11740-009-0192-y.
[8] H.N.G. Wadley, R. Mehrabian, Acoustic emission for materials processing: a review, Mater. Sci. Eng. 65 (1984) 245–263.
[9] N. Eschner, L. Weiser, B. Häfner, G. Lanza, Development of an acoustic process monitoring system for selective laser melting (SLM), in: Solid Free. Fabr. 2018 Proc. 29th Annu. Int. Solid Free. Fabr. Symp. - An Addit. Manuf. Conf. SFF 2018, 2018, pp. 2097–2117.
[10] L. Meng, B. McWilliams, W. Jarosinski, H.Y. Park, Y.G. Jung, J. Lee, J. Zhang, Machine learning in additive manufacturing: a review, Jom 72 (2020) 2363–2377, doi:10.1007/s11837-020-04155-y.
[11] J.R. Tempelman, A.J. Wachtor, E.B. Flynn, P.J. Depond, J.-B. Forien, G.M. Guss, N.P. Calta, M.J. Matthews, Detection of keyhole pore formations in laser powder-bed fusion using acoustic process monitoring measurements, Addit. Manuf. 55 (2022) 102735, doi:10.1016/j.addma.2022.102735.
[12] V. Pandiyan, R. Drissi-Daoudi, S. Shevchik, G. Masinelli, R. Logé, K. Wasmer, Analysis of time, frequency and time-frequency domain features from acoustic emissions during Laser Powder-Bed fusion process, Procedia CIRP 94 (2020) 392–397, doi:10.1016/j.procir.2020.09.152.
[13] K. Wasmer, T. Le-Quang, B. Meylan, S.A. Shevchik, In situ quality monitoring in AM using acoustic emission: a reinforcement learning approach, J. Mater. Eng. Perform 28 (2019) 666–672, doi:10.1007/s11665-018-3690-2.
[14] D. Ye, G.S. Hong, Y. Zhang, K. Zhu, J.Y.H. Fuh, Defect detection in selective laser melting technology by acoustic signals with deep belief networks, Int. J. Adv. Manuf. Technol. 96 (2018) 2791–2801, doi:10.1007/s00170-018-1728-0.
[15] S.A. Khairallah, T. Sun, B.J. Simonds, Onset of periodic oscillations as a precursor of a transition to pore-generating turbulence in laser melting, Addit. Manuf. Lett. 1 (2021) 100002, doi:10.1016/j.addlet.2021.100002.
[16] C.R. Heiple, S.H. Carpenter, Acoustic emission produced by deformation of metals and alloys - a review : Part I, J. Acoust. Emiss. 6 (1987) 177–204.
[17] L.W. Koester, H. Taheri, T.A. Bigelow, L.J. Bond, E.J. Faierson, In-situ acoustic signature monitoring in additive manufacturing processes, in: AIP Conf. Proc, 2018, doi:10.1063/1.5031503.
[18] H. Taheri, L.W. Koester, T.A. Bigelow, E.J. Faierson, L.J. Bond, In situ additive manufacturing process monitoring with an acoustic technique: clustering performance evaluation using K-means algorithm, J. Manuf. Sci. Eng. 141 (2019), doi:10.1115/1.4042786.
[19] K. Gabrysiak, T. Gustmann, J. Freudenberger, K. Neufeld, L. Giebeler, C. Leyens, U. Kühn, Development and characterization of a metastable Al-Mn-Ce alloy produced by laser powder bed fusion, Addit. Manuf. Lett. 1 (2021) 100017, doi:10.1016/j.addlet.2021.100017.
[20] P. Welch, The use of fast Fourier transform for the estimation of power spectra: A method based on time averaging over short, modified periodograms, IEEE Trans. Audio Electroacoust. 15 (1967) 70–73, doi:10.1109/TAU.1967.1161901.
[21] R. Wagner, M. Seleznev, H. Fischer, R. Ditscherlein, H. Becker, B.G. Dietrich, A. Keßler, T. Leißner, G. Wolf, A. Leineweber, U.A. Peuker, H. Biermann, A. Weidner, Impact of melt conditioning and filtration on iron-rich β phase in AlSi9Cu3 and its fatigue life studied by μCT, Mater. Charact. 174 (2021) 111039, doi:10.1016/j.matchar.2021.111039.
[22] E. Pomponi, A. Vinogradov, A real-time approach to acoustic emission clustering, Mech. Syst. Signal Process. 40 (2013) 791–804, doi:10.1016/j.ymssp.2013.03.017.
[23] C.B. Scruby, H.N.G. Wadley, J.J. Hill, Dynamic elastic displacements at the surface of an elastic half-space due to defect sources, J. Phys. D. 16 (1983) 1069–1083, doi:10.1088/0022-3727/16/6/015.
[24] V.A. Drebushchak, Thermal expansion of solids: review on theories, J. Therm. Anal. Calorim. 142 (2020) 1097–1113, doi:10.1007/s10973-020-09370-y.